Journal of Materials Chemistry A

PAPER

View Article Online
View Journal | View Issue

Cite this: J. Mater. Chem. A, 2018, 6, 14663

Synthesis of highly-active Fe–N–C catalysts for PEMFC with carbide-derived carbons†

Sander Ratso,[a] Nastaran Ranjbar Sahraie,[b] Moulay Tahar Sougrati,[b] Maike Käärik,[a] Mati Kook,[c] Rando Saar,[c] Päärn Paiste,[d] Qingying Jia,[e] Jaan Leis,[a] Sanjeev Mukerjee,[e] Frédéric Jaouen *[b] and Kaido Tammeveski *[a]

Proton exchange membrane fuel cells (PEMFC) offer a viable alternative to internal combustion engines, but highly performing stacks still require large amounts of platinum-based catalysts. Fe–N–C catalysts have recently emerged as potential substitutes. Carbide-derived carbon (CDC) can be designed to have various pore size distributions (PSD), in the microporous and/or mesoporous domains, which can be used for defining the number and/or accessibility of active sites in Fe–N–C catalysts based on the CDC. In this work, we compare two sets of Fe–N–C catalysts derived from two different CDCs, one with most frequent pore size of 8.5 Å, (CDC-2) and another one with most frequent pore sizes at 7.8 and 30 Å (CDC-1). The CDC-based Fe–N–C catalysts show excellent half-wave potential for oxygen reduction reaction (ORR) of 0.81 V *vs.* RHE in 0.5 M H_2SO_4. This work presents the first study of CDC-based catalysts in a PEMFC, where the performance of the CDC-2 based catalyst rivaled that of the best Fe–N–C materials in the literature. The catalyst derived from CDC-2 showed *ca.* 5 times higher activity at 0.8 V *vs.* RHE than the one derived from CDC-1. We show that the residual presence of boron in CDC-1 is the main reason for the lower activity of CDC-1 derived catalysts, leading to the formation of iron boride instead of ORR-active FeN_xC_y moieties. Higher Fe contents were investigated for CDC-2, but lead to unmodified activity, which is explained from Mössbauer spectroscopy measurements by the increasing formation of ORR-inactive Fe species at high Fe content. In summary, we demonstrate the excellent potential for CDC materials to be used in catalyst design and also identify some key issues that may arise from the possible residual presence of secondary atoms from the starting carbide.

Received 12th March 2018
Accepted 5th July 2018

DOI: 10.1039/c8ta02325e

rsc.li/materials-a

1. Introduction

The reduction of the impact of climate change due to the burning of fossil fuels is a major challenge. Replacing internal combustion engines in vehicles with low-temperature proton exchange membrane fuel cells (PEMFC) could significantly cut CO_2 emissions and is therefore one of the most popular topics in modern electrochemistry. For fuel cells to become a viable alternative to current technologies, however, the costs of the system need to be greatly reduced. A large part of PEMFC costs arises from the need of an active catalyst for the oxygen reduction reaction (ORR) at the cathode.[1,2] Platinum and its alloys are currently used as cathode materials in commercial fuel cell systems, but platinum is an expensive and scarce metal. Replacing Pt group-metal based cathode catalysts with non-noble metal catalysts is a promising pathway towards cheaper and more sustainable fuel cells.[1,3,4] Porous carbon materials have multiple desirable properties for fuel cell electrodes, such as a high specific surface area, high electrical conductivity and relatively good chemical and mechanical stability. Therefore, the doping of porous carbons has emerged as a possible approach to activate them towards the ORR, with the ultimate goal of replacing Pt-based catalysts.[5–7] The nature of the active sites for the ORR on non-noble metal catalysts prepared from metal, nitrogen and carbon precursors at high temperature has been a matter of debate since its inception, about half a century ago.[8] In recent years, comprehensive electrochemical and spectroscopic studies have identified three main types of sites for O_2 electroreduction in acidic media on Fe–N–C catalysts: iron-nitrogen moieties covalently integrated at the surface of a conductive carbon matrix (FeN_xC_y sites),[9–12] metallic particles encapsulated in nitrogen-doped carbon ($Fe@N_xC_y$ sites)[13] and

[a]Institute of Chemistry, University of Tartu, Ravila 14a, 50411 Tartu, Estonia. E-mail: kaido.tammeveski@ut.ee; Fax: +372-7375181; Tel: +372-7375168

[b]Institut Charles Gerhardt Montpellier, Laboratory for Aggregates, Interfaces and Materials for Energy, UMR 5253, CNRS, Université de Montpellier, ENSCM, 34095 Montpellier, France. E-mail: frederic.jaouen@univ-montp2.fr

[c]Institute of Physics, University of Tartu, W. Ostwald Str. 1, 50411 Tartu, Estonia

[d]Institute of Ecology and Earth Sciences, University of Tartu, Vanemuise 46, 51014 Tartu, Estonia

[e]Department of Chemistry and Chemical Biology, Northeastern University, Boston, MA, 02115, USA

† Electronic supplementary information (ESI) available. See DOI: 10.1039/c8ta02325e

nitrogen functional groups on the carbon surface (N_xC_y sites).[14–16] FeN_xC_y moieties incorporated into a defective carbon layer are usually considered the most active site. Their exact geometry and pathways for the ORR have also been extensively discussed.[12,13,17–20] For $Fe@N_xC_y$ catalysts, the role of iron has been found to be rather different from FeN_xC_y active sites since Fe does not directly partake in the ORR, but rather changes the stability of intermediates on the nitrogen-doped carbon surface. N_xC_y sites, in turn, can differ according to the exact position of nitrogen in the carbon lattice, with pyrrolic N debated to catalyse the oxygen reduction into hydrogen peroxide and pyridinic N catalysing the reduction of hydrogen peroxide into water, as discussed by Artyushkova *et al.*[18] Still, even with a high amount of pyridinic nitrogen, the ORR activity of metal-free catalysts is very low. The idea of pyridinic-N catalysing H_2O_2 reduction to water has been recently disputed by measuring the activity for peroxide reduction in acidic media of a set of materials containing either N_xC_y, $Fe@N_xC_y$ or FeN_xC_y.[21] It was concluded that both $Fe@N_xC_y$ and FeN_xC_y can reduce peroxide to water (although the reaction is sluggish) while N_xC_y groups (pyrrolic, pyridinic or graphitic N) cannot.[21] Other activity descriptors for ORR include the surface basicity,[11] degree of disorder in the support carbon material[17,22] and microporosity[9,23,24] of the catalyst.

To prepare an active Fe–N–C catalyst, then, one has to incorporate as many active sites as possible into a carbon material, while still retaining high conductivity, mass transport and chemical stability under fuel cell conditions. Three main methods for achieving highly active Fe–N/C catalysts have been developed: (i) the sacrificial metal–organic framework (MOF) approach,[9,11,25,26] where iron and nitrogen-containing precursors are pyrolysed after introducing them into or around MOF crystals, (ii) the sacrificial support method (SSM), where the C, N and Fe precursors are infiltrated in and around a porous template material such as porous silica, and the template removed in a post-pyrolysis etching step,[18,27] providing control over the mesoporosity and (iii) the pyrolysis of a nitrogen-containing molecule or polymer in the presence of Fe precursor.[28–32] All of these methods have their advantages, such as a very high starting surface area for the MOF-based method, facile control over the porosity and structure of the product for the SSM method and evenly and highly dispersed nitrogen moieties for the N-containing polymer approach.

One drawback to all those approaches is however the lack of precise control of the pore size distribution (PSD), especially in the microporous region (pore size $\leq$ 2 nm). The latter is typically engendered by the transformation of organic precursors into more or less graphitic domains, *e.g.* MOFs lose their crystalline structure and lose many Zn, N and C atoms as volatile products during pyrolysis. This applies to polymer or monomer pyrolysis, and to the organic precursors infiltrated in porous silica as well. Thus, while some control has been gained on mesopores (SSM method, or addition of carbon black in the polymer approach), little control is available to tune the quantity and size of micropores in Fe–N–C materials. This is unsatisfactory, especially since the micropore surface area in Fe–N–C materials has, on many instances, been positively correlated with ORR activity in acid medium.[31,33–35]

Carbide-derived carbons (CDC) can offer a control on the porosity of the carbon material, from narrow to wide pore size distributions in both the micro- and mesoporous domains. They are produced by removing metal atoms from a carbide lattice *via* chlorination and are already applied in commercial supercapacitors, due to their high specific surface area (SSA) over 2000 $m^2\ g^{-1}$ and porosity.[36] The surface area, degree of disorder and pore size distribution are easily tuneable by selection of starting carbide and chlorination temperatures[37,38] ranging from α-SiC-based carbon with a median pore diameter of ~0.7 nm and virtually only microporosity to Mo_2C-derived carbon, which can have a median pore diameter of ~4.0 nm and no micropores at all[39] with reproducible large-scale results.[40] CDCs are thus promising as a microporous host for Fe-based sites. Because the structure of the final Fe–N–C catalyst may be governed by the morphology of the carbon substrate,[41] the control over the porosity and structure of the CDCs may open the path for the synthesis of Fe–N–C catalysts with selected pore size, and perhaps *in fine* selected type of FeN_xC_y moieties.

In this work, we investigate the effect of PSD in CDCs on the morphology, Fe coordination and ORR activity of Fe–N–C catalysts in acid derived from two different CDCs. The structure and composition of the electrocatalysts are studied using N_2-sorption, X-ray photoelectron spectroscopy (XPS), X-ray diffraction (XRD), X-ray absorption spectroscopy (XAS) and ^{57}Fe Mössbauer spectroscopy. The ORR activity is explored with the rotating disk electrode (RDE) method. The most active catalyst materials are also characterised in a single-cell PEMFC. We show that while both CDCs resulted in fairly active Fe–N–C catalysts, the CDC-2 with unimodal PSD centred in the micropore region resulted in Fe–N–C catalysts with a 5 times higher ORR activity. Also, while the PSD was similar in both Fe–N–C catalysts and revealed mostly micropores (in contrast to different PSD of the starting CDC-s), Mössbauer spectroscopy identifies that the Fe species formed during pyrolysis was very different with CDC-1 and CDC-2, for structural reasons (PSD) but also mainly for chemical reasons (composition of CDC – residual element from the starting carbides, in particular boron). These novel insights will help design novel Fe–N–C catalysts by linking structure and chemical purity in the templating carbide-derived carbon to the preferential formation of ORR-active FeN_xC_y moieties during pyrolysis.

2. Experimental

2.1. Synthesis of carbide-derived carbons (CDC)

For the synthesis of CDC-1, boron carbide powder (B_4C, H. C. Starck, Ø < 0.8 μm) was placed into a horizontal quartz-tube reactor and was treated with chlorine gas (2.8, AGA) at a flow rate of 1.5 L min^{-1} at 1000 °C for 260 min. After that, the CDC powder formed was annealed in argon (4.0, AGA, 2 L min^{-1}) flow at 1000 °C for 1 h and dechlorinated in hydrogen (4.0, AGA, 1 L min^{-1}) flow at 800 °C for 6.5 h.

For the synthesis of CDC-2, titanium carbide powder (TiC, H. C. Starck, Ø < 4 μm) was placed into a horizontal quartz-tube reactor and was treated with chlorine gas (2.8, AGA) at a flow rate of 1.5 L min^{-1} at 900 °C. After that, the reactor was heated up to 1000 °C and flushed with argon (4.0, AGA, 1 L min^{-1}) to remove the excess of chlorine and other gaseous by-products from carbon. The deep dechlorination of CDC powder was done using hydrogen (4.0, AGA, 1 L min^{-1}) flow at 800 °C. After synthesis a physical post-activation of the CDC powder, described in detail elsewhere,[42] was performed at 900 °C with argon/water vapour to the carbon weight loss of 40%.

2.2. Synthesis of Fe–N–C materials from CDC

Carbide-derived carbon powders produced from titanium carbide and boron carbide were received from Skeleton Technologies OÜ (Estonia). In a typical synthesis, 200 mg of CDC along with 50 mg of 1,10-phenanthroline and the appropriate mass of iron(II) acetate to reach either 0.5, 1 or 2 wt% Fe in the overall catalyst precursor before pyrolysis (*e.g.* 8 mg iron(II) acetate for 1 wt% Fe in catalyst precursor) were weighed and placed into a ZrO_2 planetary ball mill with 100 ZrO_2 balls of 5 mm diameter and ball-milled for 4 segments of 30 min with 5 min cool down periods between each segment at a rotation rate of 400 rpm. The resulting powder was then pyrolysed in a quartz tube oven at 800 °C under Ar flow for 1 h. The pyrolysis duration at 800 °C was controlled by quickly inserting the quartz boat into the heating zone using a magnet, and removing the tube from the oven after 1 h had passed. The catalysts are named in the following text by their iron content before pyrolysis and precursor type. For example, the boron carbide derived catalysts with 1.0 wt% of iron in the catalyst precursor before pyrolysis has the designation Fe_1–N/CDC-1.

2.3. Physical characterisation of Fe–N/C catalysts

The morphology of the Fe–N–C catalysts was studied using scanning electron microscopy (SEM). The SEM micrographs were recorded with Helios™ NanoLab 600 (FEI) with various magnifications to examine both the larger morphology and microstructure. For preparing the SEM samples, a suspension of the catalyst in isopropanol was pipetted onto a polished glassy carbon disk. The elemental concentration in the catalyst materials was determined using energy-dispersive X-ray (EDX) microanalysis *via* Helios NanoLab 600 electron-ion dual beam microscope equipped with 50 mm^2 X-Max silicon drift detector (Oxford Instruments). The energy of primary electrons was 10 keV. The EDX spectra were analysed using the standard procedures provided by INCA software (Oxford Instruments).

The elemental composition of the surface of the catalysts was analysed using X-ray photoelectron spectroscopy (XPS) *via* the SCIENTA SES-100 spectrometer. The samples were prepared by dispersing 2 mg of the catalyst materials in ethanol and pipetting them onto polished Si wafer. The catalysts were examined using a non-monochromatic twin anode X-ray tube (XR3E2), where the characteristic energies were 1253.6 eV (Mg $K\alpha_{1,2}$, FWHM 0.68 eV) and 1486.6 eV (Al $K\alpha_{1,2}$, FWHM 0.83 eV). The pressure in the analysis chamber was below 10^{-9} torr and the source power was 300 W. The survey scan was collected using the following parameters: energy range = 800 to 0 eV, pass energy = 200 eV, step size = 0.5 eV. The high resolution scans were conducted using pass energy 200 eV and step size 0.1 eV. The N 1s XPS peak was deconvoluted to 6 components:[43,44] (i) pyridinic N, (ii) pyrrolic N, (iii) and (iv) graphitic N, (v) Fe–N_x and (vi) pyridine-N-oxides. On average the peak binding energy positions were found to be: (i) 398.5 eV, (ii) 400.8 eV, (iii) 401.5 eV, (iv) 402.4 eV, 399.8 eV (v) and (vi) 404.5 eV. The spectra were calibrated after the C 1s peak position to 248.8 eV. FWHM was constricted from 1.3 eV to 1.8 eV for peaks (i)–(v) and 1.5 eV to 2.5 eV for peak (vi). Peak positions were constricted at: (i) 399.6–398.4 eV, (ii) 400.9–400.7 eV and (vi) 410–404.5 eV. Peaks (iii)–(v) had their positions fixed in relation the pyridinic peak: (iii) +3 eV, (iv) +3.9 eV and (v) +1.3 eV based on DFT calculations.[43,44] All peaks were assumed to be 70% Gaussian and 30% Lorentzian. Shirley backgrounds were used. The software CasaXPS (2.3.18) was used for peak fitting.

For determining the bulk concentration of elements in the catalysts, ICP-MS was used. Sample digestion, prior to analysis with ICP-MS was performed with Anton Par Multiwave PRO microwave digestion system using NXF100 digestion vessels (PTFE-TFM liner) in 8 N rotor. 10 mg of sample was weighed into PTFE vessels and 3 mL of HNO_3 (Carl Roth ROTIPURAN Supra) along with 3 mL of H_2O_2 (Fluka TraceSELECT Ultra) were slowly added to the vessel. After the initial vigorous reaction had subsided 1 mL of HF (Carl Roth ROTIPURAN Supra) was added, the vessels were capped and digested in the microwave unit. A stepwise power controlled digestion procedure for 8 vessels was employed: ramp to 600 W in 10 min, ramp to 1000 W in 8 min, ramp to 1500 W in 8 min, hold at 1500 W for 30 min. It was observed during method development that temperatures in excess of 200 °C were needed for complete digestion. After digestion the samples were diluted using 2% HNO_3 solution (prepared from 69% HNO_3 Carl Roth ROTIPURAN Supra) to a final dilution factor of 70 000 and analysed using Agilent 8800 ICP-MS/MS. ^{11}B, ^{90}Zr and ^{47}Ti were measured using NoGas mode in MS/MS "on mass" configuration and ^{56}Fe, ^{57}Fe were measured using MS/MS "on mass" configuration with He (6 mL min^{-1}) as collision gas in the CRC (collision-reaction cell). For the samples synthesized with natural iron, ^{56}Fe was used to quantify the iron content assuming natural distribution of iron isotopes, otherwise ^{57}Fe was used, assuming 95% abundance of ^{57}Fe.

N_2 adsorption/desorption isotherms of the catalyst samples were recorded at 77 K using a NovaTouch LX2 Analyser (Quantachrome). The samples were dried under vacuum at 200 °C for two days and at 300 °C for 12 h to remove any volatile guest molecules and backfilled with N_2 gas before the measurement. The catalysts' specific surface area (S_{BET}) was calculated according to the Brunauer–Emmett–Teller (BET) theory up to a nitrogen relative pressure of $P/P_0 = 0.2$. The total volume of pores (V_{tot}) was measured near to saturation pressure of N_2 ($P/P_0 = 0.97$). The average diameter of pores (d_p) was calculated for a slit-type pore geometry using the following equation: $d_p = 2V_{tot}/S_{BET}$. The calculations of pore size distribution (PSD), microporosity (V_μ) and surface area (S_{DFT}) from N_2 isotherms

were done by using a quenched solid density functional theory (QSDFT) equilibria model for slit type pore.

Ex situ XAS measurements on the sample with the sample loading reaching a ~0.05 edge height at the Fe K edge were collected in the fluorescence mode at the beamline 8-ID at the NSLS-II, Brookhaven National Laboratory. Multiple scans were collected to increase the signal-to-noise ratio, and to ensure the repeatability of the data. Scans were calibrated, aligned, merged and normalised with background removed using the IFEFFIT suite.[45] X-Ray Diffraction (XRD) characterisation was conducted using a PANanalytical X'Pert powder X-ray diffractometer and using the Cu K_α radiation.

2.4. Electrode preparation and electrochemical characterisation

For measuring the ORR activities of the Fe–N–C catalysts, the rotating disk electrode (RDE) method was employed. For electrode preparation, 10 mg of the catalyst material was dispersed in a mixture of 108 μL of 5 wt% Nafion solution in ethanol containing 15–20% water, 37 μL of H_2O and 300 μL of pure ethanol. A 7 μL aliquot of the resulting ink was deposited on a glassy carbon (GC) disk electrode (Pine Research, Grove City, PA, USA) with a surface area of 0.196 cm^2 that had previously been polished with alumina slurries (Buehler) with a grain size of 1 and 0.05 μm and ultrasonically cleaned in deionized water twice. This results in a catalyst loading of 0.8 mg cm^{-2}. The experiments were carried out in a three-electrode electrochemical cell filled with 0.5 M H_2SO_4 (95–97%, Sigma-Aldrich). Prior to the experiments, the electrolyte solution was saturated with O_2 or N_2 (for background current correction) and a gas flow over the electrolyte surface was maintained during the electrochemical experiments. A graphite rod served as the counter electrode and a reversible hydrogen electrode (RHE) as the reference electrode. The ORR polarisation curves were recorded at a rotation rate of 1600 rpm and at a scan rate (ν) of 10 mV s^{-1} from 1 to 0 V *vs.* RHE. Prior to recording the polarisation curves, ten potential cycles were done at a scan rate of 100 mV s^{-1} from 1 to 0 V for pre-conditioning of the electrode. A 5 wt% Pt/C (Johnson Matthey) catalyst was used for comparison. The Pt/C ink consisted of 20 mg of 5 wt% Pt/C dispersed in a mixture of 108 μL of 5 wt% Nafion solution in ethanol containing 15–20% water, 37 μL of H_2O and 300 μL of pure ethanol. 4 μL of the catalyst was deposited on the GC electrode yielding Pt loading of 20 μg_{Pt} cm^{-2}. All inks were sonicated at least for an hour to achieve a homogenous suspension. A VersaStat 3 potentiostat from Princeton Applied Research (PAR) was used for the experiments. To study the stability of $Fe_{0.5}$–N/CDC-2, an electrode was prepared similar to the ORR activity RDE test. First, the ORR activity in O_2-saturated 0.5 M H_2SO_4 was measured, after which 10 000 potential cycles between 0.925 and 0.6 V *vs.* RHE in Ar-saturated solution were undertaken and then the ORR activity was measured again.

2.5. MEA fabrication and fuel cell measurement

For MEA fabrication, the ink formulation was the following: 20 mg of Fe–N–C cathode catalyst material mixed in 652 μL of 5 wt% Nafion solution containing 15–20% water, 326 μL of pure ethanol and 272 μL of water. Then the inks were deposited on a clean gas-diffusion layer (Sigracet S10-BC) in 400 μL aliquots. The cathodes were dried at 80 °C for at least 2 h. The anode used for all PEMFC tests was a commercial Pt/C catalyst with a loading of 0.5 mg_{Pt} cm^{-2} on Sigracet S10-BC. The MEAs were prepared by hot-pressing the anode and cathode (both 4.84 cm^2) on a Nafion NRE-211 membrane at 135 °C for 2 min using a force of 500 lb. The MEAs were then sandwiched in a single-cell (Fuel Cell Technologies, USA) using a torque of 10 Nm. A Biologic potentiostat with 50 A load in an in-house fuel cell testing station and EC-Lab software were used to evaluate MEA performance of the catalysts, while the temperature of a fuel cell was kept at 80 °C. Pure O_2 was used on the cathode and pure H_2 on the anode side of PEMFC. The gases were pre-humidified to 100% RH. The cell temperature was 80 °C during the measurements and the humidifiers were kept at 90 °C to ensure 100% RH. A reference measurement using the same conditions, but a 5 wt% Pt/C cathode catalyst with a loading of 80 μg_{Pt} cm^{-2}, was also conducted.

3. Results and discussion

3.1. Physical characterisation of the CDCs and Fe–N–C materials

A study of the surface morphology of the Fe–N–C catalysts was undertaken using scanning electron microscopy (SEM) to understand the changes in the structure of the catalyst after the nitrogen and iron doping. Fig. 1a shows the morphology of the B_4C-derived carbon material (CDC-1) and Fig. 1b the morphology of the TiC-derived carbon material (CDC-2). CDC grains of various sizes are visible, all of them showing a disordered carbon structure. CDC-2 has a larger grain size than CDC-1, which dictates the final particle size of the catalysts derived from it. Fig. 1c and d show the morphology of Fe_1–N/CDC-1 and

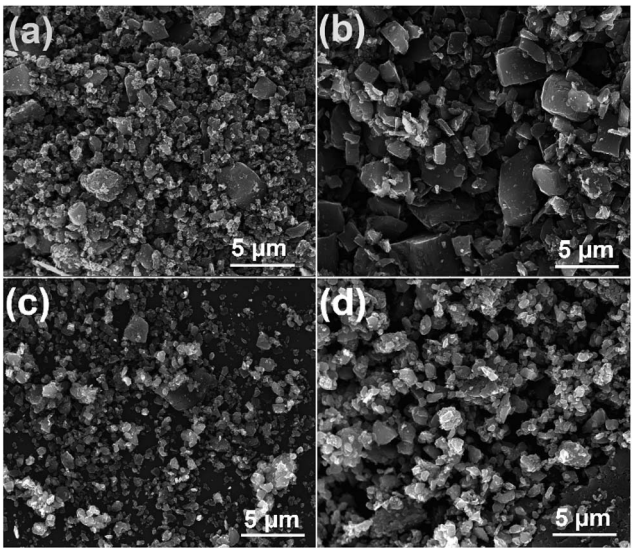

Fig. 1 SEM micrographs of CDC-1 (a), CDC-2 (b), Fe_1–N/CDC-1 (c) and Fe_1–N/CDC-2 (d) materials.

Fe_1–N/CDC-2, respectively. Fe_1–N/CDC-1 shows a SEM image similar to that of the parent material, CDC-1. The doped CDC particles are mostly sized around 500 nm, with some agglomerates in the micrometre size range and some smaller particles of around 100 nm. Fe_1–N/CDC-2 has also visibly retained a macro-structure similar to that of the parent material, CDC-2. The particle size has decreased somewhat, probably due to the ball-milling, but it is still larger than that of Fe_1–N/CDC-1.

The textural properties of both the starting materials and the Fe–N–C catalysts are given in Table 1. The main difference between the two starting CDC materials was in the pore size distribution, which is also demonstrated in Fig. S1.† The CDC-1 material has a trimodal micro-mesoporous structure with a large amount of mesopores and micropores, while CDC-2 has a unimodal pore size distribution centred at 0.85 nm. The average pore diameter was also accordingly higher for CDC-1 (1.65 nm) compared to CDC-2 (1.05 nm).

As there have been various studies claiming that either micropores, mesopores or a combination of both are needed for efficient Fe–N–C catalysts,[23,33,34,46–48] these CDCs might present an interesting opportunity to study the effect of PSD on Fe–N–C catalyst activity. However, the PSD of two Fe–N–C catalysts with 1 wt% Fe and prepared identically except for the carbon support (CDC-1 and CDC-2) are quite similar (see Fig. 2a and b), in spite of drastically different PSD of the starting CDCs.

It is apparent from Table 1 that, after ball-milling and pyrolysis in Ar, the specific surface area decreased by about 750–1200 $m^2\ g^{-1}$. This may be explained either as a filling of the pores with phenanthroline and Fe acetate or as partial graphitization of the disordered carbon in CDC during the high-temperature pyrolysis. Iron nanoparticles are known to graphitize disordered carbon materials at high temperatures,[49,50] thus closing off some of the pores and decreasing the BET surface area. The effect of Fe content on catalyst morphology and PSD was investigated only for CDC-2 (Table 1) since a much higher ORR activity was observed with CDC-2 derived Fe–N–C catalysts (see later). The effect of Fe content on decreased BET area is however unlikely the major effect at work here since even $Fe_{0.5}$–N/CDC-2, which has a minimum amount of particulate iron according to Mössbauer spectroscopy (see later), has a specific area of 945 $m^2\ g^{-1}$, much lower than the starting area of 1997 $m^2\ g^{-1}$ for CDC-2. Also, increasing the iron content from 0.5 to 2 wt% in the pre-pyrolysis mixture results in a decrease of SSA of only about 250 $m^2\ g^{-1}$, with all three Fe–N–C catalysts derived from CDC-2 having a BET area much lower than that of CDC-2 (Table 1).

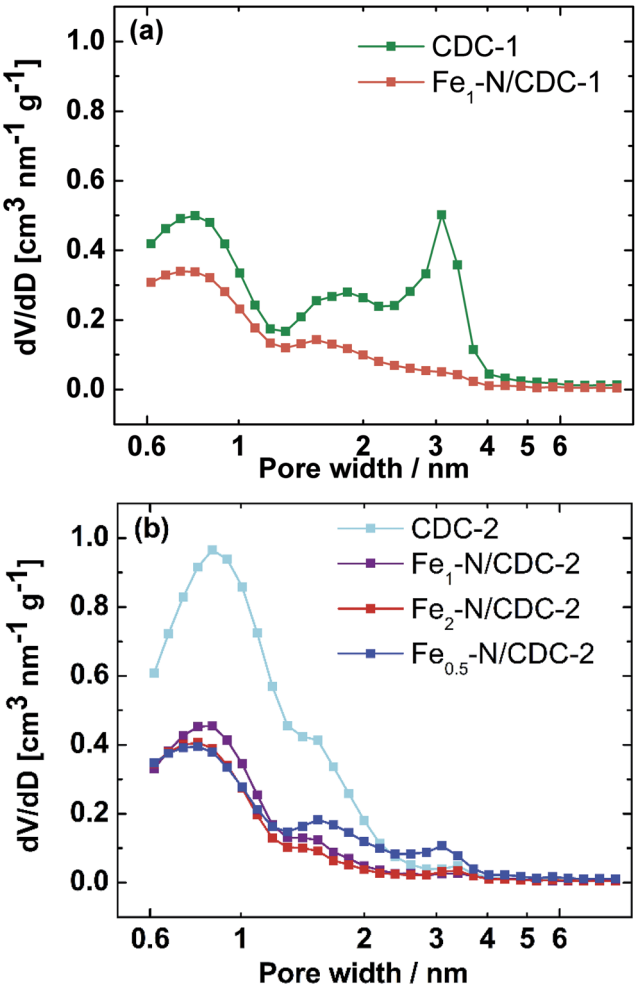

Fig. 2 Comparison of pore size distributions for CDC-1 and CDC-1 derived catalysts (a), and for CDC-2 and CDC-2 derived catalysts (b).

In our previous work, we used dicyandiamide (DCDA), Fe and Co salts to dope microporous CDC materials, where the micropore volume of M–N–C catalysts relative to the starting CDC even increased by *ca.* 0.2 $cm^3\ g^{-1}$ during the doping procedure.[51] The decrease in surface area observed here is thus much larger than that in our previous work. It can be proposed that 1,10-phenanthroline either fills the pores more effectively than DCDA, or that it transforms into residual carbon to a higher extent than DCDA. It is also possible that, contrary to DCDA, 1,10-phenanthroline blocks the pore entrances and in the end, most of the inner porosity is not accessible for

Table 1 Textural properties of CDC and Fe–N/CDC materials: BET surface area (S_{BET}), total pore volume (V_{tot}), average pore size (d_p), surface area (S_{DFT}) and micropore volume (V_μ) calculated from the QSDFT model

Sample	S_{BET}, $m^2\ g^{-1}$	V_{tot}, $cm^3\ g^{-1}$	d_p, nm	S_{DFT}, $m^2\ g^{-1}$	V_μ, $cm^3\ g^{-1}$
CDC-1	1493	1.236	1.65	1351	0.470
Fe_1–N/CDC-1	754	0.471	1.24	716	0.292
CDC-2	1997	1.057	1.05	1759	0.811
Fe_1–N/CDC-2	798	0.466	1.17	770	0.321
Fe_2–N/CDC-2	706	0.427	1.21	709	0.280
$Fe_{0.5}$-N/CDC-2	945	0.704	1.48	1009	0.397

electrocatalysis. Looking more closely at the changes in PSD from CDC to Fe_1–N/CDC, it can be seen that, with CDC-1, mesopores are nearly completely filled along with a small amount (*ca.* 30%) of micropores while for CDC-2 *ca.* 55–60% of the micropore volume is lost. This is likely due to the preferential filling of mesopores by phenanthroline in CDC-1, while with CDC-2 only micropores are present and therefore all the phenanthroline added during the synthesis fills those pores.

A summary of the XPS results for all catalysts is given in Table 2. Interestingly, the nitrogen content for the 1% Fe catalyst based on CDC-1 (Fe_1–N/CDC-1) was slightly higher than for the corresponding catalyst based on CDC-2 (Fe_1–N/CDC-2). This may be connected with the higher disorder of carbon in Fe_1–N/CDC-1, but also with the residual presence of boron in CDC-1, as will be shown later. It is known that co-doping of carbon materials by N and B usually leads to higher nitrogen content.[52] However, the relative contents of all the different nitrogen species were very comparable for all catalysts. The nitrogen content in CDC-2 based materials decreased by 0.5 at% with increasing Fe content in the catalyst precursor from 0.5 to 2 wt%, but the relative content of the N_x–Fe component was nearly the same. Unfortunately, the Fe content and speciation could not be determined by XPS due to low signal-to-noise ratio at the Fe 2p level. All N 1s high-resolution spectra are presented in Fig. 3.

Fig. 4 shows the XRD patterns of Fe–N/CDC samples. The ZrO_2 contamination in CDC-1 based materials is clearly visible, while there is no ZrO_2 contamination in CDC-2-derived catalysts. The 002 reflection of graphite 2H or 111 reflection of rhombohedral graphite, at $2\theta \approx 26.2$–$26.6°$, is present in the diffraction patterns of both CDC materials, but after the doping procedure, it becomes broader with a shoulder developing on the lower angles (more visible for CDC-2 derived materials). This effect is possibly associated with the microporous carbon becoming amorphous as the catalyst is milled or pyrolyzed. For CDC-2, increasing the iron content in the catalyst precursor mixture results in more intense diffraction peaks assigned to graphite, iron carbide and α-Fe, as expected due to the graphitization of disordered carbon by iron.[49] The broad XRD peak at $2\theta \approx 41$–$46°$, assigned to the 100 and 101 reflections of graphite 2H and/or 010 and 110 reflections of rhombohedral graphite, is present in all catalyst samples. To be noted is the surprising presence of ZrO_2 in the CDC-1 based materials, which is further discussed under the ICP-MS results section. Also, CDC-2 seems to contain some α-Fe impurity (characteristic peak at 43.6 and 50.8°).

The ^{57}Fe Mössbauer spectra of the Fe–N–C catalysts derived from CDC-1 and CDC-2 were collected for a Fe content of 0.5 wt% in the catalyst precursor. The low Fe content allows a better observation of quadrupole doublets that are assigned to FeN_xC_y moieties. The effect of Fe content on the Fe speciation in CDC-2 derived materials (selected due to their higher ORR activity, see later) was then investigated by measuring the spectra of the materials Fe_1–N/CDC-2 and Fe_2–N/CDC-2 as well. The Mössbauer spectra are presented in Fig. 5. Compared to commonly reported spectra for Fe–N–C catalysts, the spectrum of $Fe_{0.5}$–N/CDC-1 (Fig. 5a) is unusual, especially for a catalyst with such a low Fe content, and was fitted with a doublet and a sextet with unusual parameters. While the doublet has Mössbauer parameters similar to D1 commonly observed in ORR-active Fe–N–C catalysts, the sextet has, to the best of our knowledge, never been reported before in such catalysts. The average value of the sextet parameters (Table S1†) are very similar to those reported for iron boride FeB with a hyperfine field of 9.5 tesla.[53,54]

The formation of FeB is in agreement with the presence of boron in CDC-1 derived catalyst (see discussion on presence of boron later in the ICP-MS results section). Concerning the CDC-2 derived catalysts (Fig. 5b–d), we observe a broad doublet assigned to superparamagnetic Fe-based (sub-)nanoparticle (labelled SP). The assignment of the broad SP doublet to Fe nanoparticles is supported by EXAFS measurements on $Fe_{0.5}$–N/CDC-2 (Fig. 6). Apart from this, the spectra of CDC-2 derived

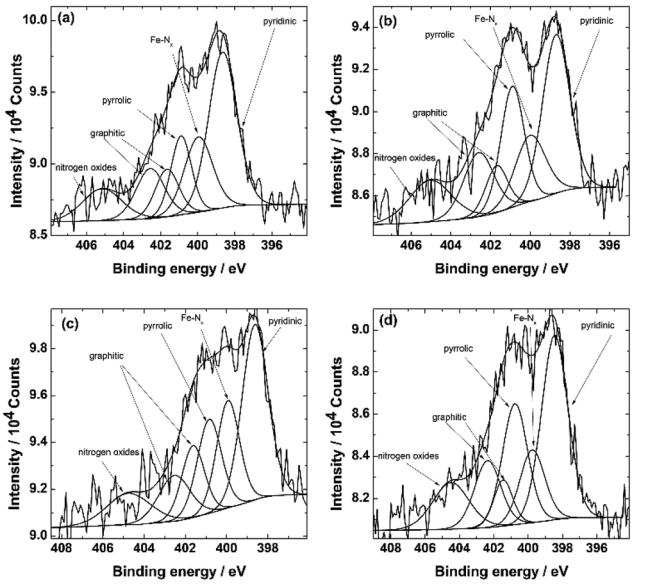

Fig. 3 Core-level XPS spectra in the N 1s region for (a) Fe_1–N/CDC-1, (b) Fe_1–N/CDC-2, (c) Fe_2–N/CDC-2 and (d) $Fe_{0.5}$-N/CDC-2.

Table 2 Overall nitrogen content and the relative nitrogen moiety concentration in the catalyst surface layers as determined by XPS

	Total N content	Fe–N_x%	N–O%	Graphitic (1)%	Graphitic (2)%	Pyridinic%	Pyrrolic%
Fe_1–N/CDC-1	1.9 at%	12	10	7	11	39	21
Fe_1–N/CDC-2	1.3 at%	11	12	6	14	33	25
Fe_2–N/CDC-2	1.1 at%	12	10	10	10	35	23
$Fe_{0.5}$-N/CDC-2	1.6 at%	13	12	6	12	35	22

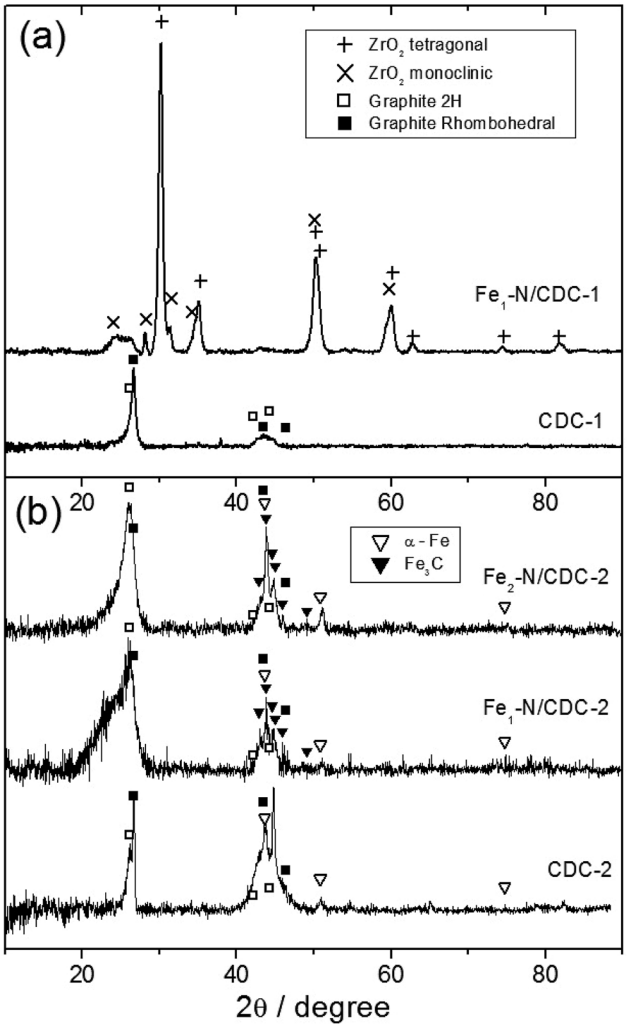

Fig. 4 XRD diffraction patterns for Fe–N/CDC and undoped CDC samples based on (a) CDC-1 and (b) CDC-2. The position of the main diffraction peaks are indicated for graphite 2H (JCPDS 01-075-1621), rhombohedral graphite (JCPDS 01-075-2078), ZrO_2 tetragonal (JCPDS 01-079-1769), ZrO_2 hexagonal (JCPDS 00-037-1484), α-Fe (JCPDS 96-900-8470) and Fe_3C (JCPDS 01-085-1317).

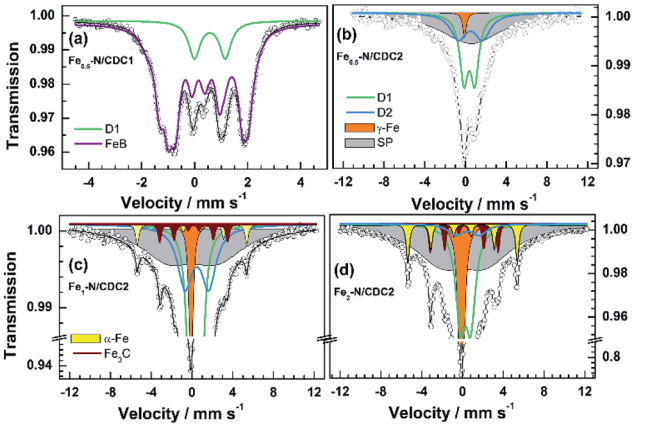

Fig. 5 Room temperature ^{57}Fe Mössbauer spectra of (a) $Fe_{0.5}$–N/CDC-1, (b) $Fe_{0.5}$–N/CDC-2, (c) Fe_1–N/CDC-2, (d) Fe_2–N/CDC-2. For (c) and (d), note that the *Y*-axis scale is broken in order to improve the visibility of the low intensity components of magnetic Fe (sextets) and of the doublets.

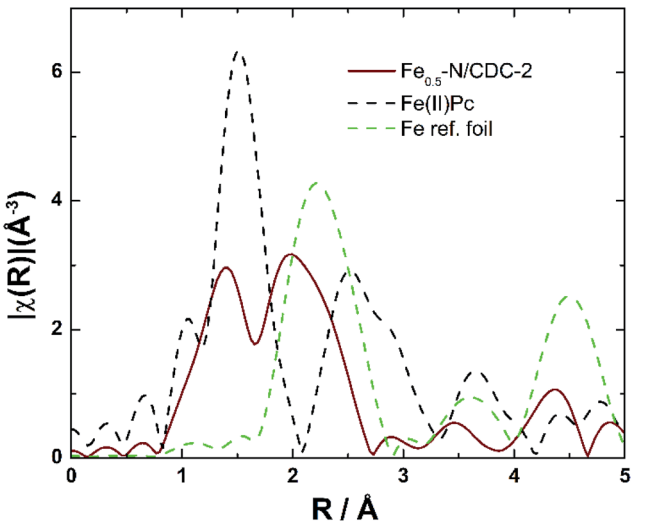

Fig. 6 The FT-EXAFS of the sample $Fe_{0.5}$–N/CDC-2, Fe(II)Pc, and iron reference foil (intensity reduced by a factor of 6 for the Fe foil, for comparison purpose).

samples can be fitted with components usually observed in pyrolysed Fe–N–C catalysts, namely D1, D2, α-Fe, γ-Fe and Fe_3C. It can be seen from Fig. 5 and Table S2† that the total absorption (%) of α-Fe, γ-Fe, Fe_3C increases with increasing amount of iron precursor on CDC-2. In summary, the striking difference between CDC-1 and CDC-2 derived catalysts (at 0.5% Fe level) is the low% area (13%) assigned to D1 in $Fe_{0.5}$–N/CDC-1 and the major presence of FeB, while $Fe_{0.5}$–N/CDC-2 comprised a large amount of doublets D1 and D2 (48%).

The co-presence of the FeN_xC_y and inorganic Fe species with relatively high content is verified by ex situ X-ray absorption spectroscopy (XAS). As seen in Fig. 6, the FT-EXAFS of the $Fe_{0.5}$–N/CDC-2 contains a scattering peak around 1.5 Å (without phase correction), overlapping the peak of Fe(II)Pc arisen from the first shell Fe–N scattering; as well as a scattering peak around 2 Å overlapping the first shell Fe–Fe scattering peak in metallic Fe. The high intensity of the Fe–Fe scattering peak supports the presence of high amount inorganic Fe species in the catalyst, which can be linked to the broad SP contribution.

The contents of Fe, B, Ti and Zr in the catalyst materials with 1% Fe at synthesis stage (baseline Fe content) were determined *via* ICP-MS. Obviously, Fe_1–N/CDC-1 has a large content of ZrO_2 compared to smaller amounts present in the samples synthesized using CDC-2. This is likely due to the fact that there is a rather large amount of B_4C still present in CDC-1 when compared to TiC content in CDC-2, as supported by the high content of B in CDC-1-derived material but low Ti content in CDC-2-derived materials. During the chlorination process, some of the carbide precursor (B_4C or TiC in this case) can get trapped inside the carbon. As B_4C and TiC are very hard (Mohs hardness of approximately 9–10 and 9–9.5, respectively) even compared to ZrO_2 (Mohs hardness of ~8), it is probable that,

during the ball-milling process, the ZrO_2 balls and crucible are eroded by the sample, resulting in Zr contamination. The erosion effect also means that a small amount of boron is milled into the jar and balls themselves and can be transferred to other samples. Since Fe_1–N/CDC-1 has a larger amount of carbide particles still present, the resulting Zr content is also consequently higher. Regarding the iron contents, Fe_1–N/CDC-2 contained surprisingly nearly twice more iron than Fe_1–N/CDC-1, while both had the same amount of iron in the catalyst precursor mixture. For CDC-2 materials, the Fe content in catalysts increased linearly with Fe content in the precursors. It is to be noted that the iron concentrations are likely somewhat underestimated here due to the lack of a suitable reference material to confirm the total dissolution of the determined elements from the sample.

3.2. Electrocatalytic activity of the Fe–N/CDC catalysts towards the ORR

The Fe–N/CDC materials were first investigated using the RDE setup for assessing the catalytic activity toward the ORR in acid. Fig. 7 shows the ORR activity of the CDC-derived Fe–N/CDC materials along with the starting CDC, measured in O_2-saturated 0.5 M H_2SO_4 solution. The electrolyte was 0.5 M H_2SO_4 for Fe–N/CDC catalysts, but for comparison, 0.1 M $HClO_4$ was used for the Pt/C material to avoid activity loss caused by bisulphate adsorption on Pt.[55] Modifying the CDC materials with iron and nitrogen shifts positively the onset potential (E_{onset}, defined as the potential at 0.2 mA cm^{-2}) nearly 300 mV, showing a massive increase in the ORR electrocatalytic activity. Also, the half-wave potential ($E_{1/2}$) for O_2 reduction shifted from *ca.* 0.4 to *ca.* 0.8 V *vs.* RHE. The rise in activity is due to a large amount of Fe–N_x centres formed in the pores of the CDC materials during the pyrolysis procedure, while both starting CDCs have very low ORR activity themselves. The $E_{1/2}$ values and j_k at 0.8 V *vs.* RHE along with the mass activity (MA) of the Fe–N–CDCs and other state-of-the-art Fe–N–C catalysts are given in Table 4. The kinetic current densities were calculated using the Koutecky–Levich equation: $j_k = j_d \times j/(j_d - j)$, where j_d was taken as the limiting current density at 0.5 V *vs.* RHE.

Next, the RDE results show that Fe_1–N/CDC-2 has a higher ORR activity than Fe_1–N/CDC-1. Remarkably, both the values of E_{onset} and $E_{1/2}$ were almost identical for all three CDC-2 based catalysts, showing no significant dependence of overall ORR activity on the iron content in the range of 0.5–2% Fe in the precursor (0.49 to 1.45 wt% Fe in catalysts, see Table 3). Although the iron content rose by 0.95 wt% when going from 0.5 wt% to 2 wt% of iron in the CDC-2 catalyst precursors, the relative% of iron in the form of D1 and D2 species (the ORR-active species) decreased from 48% to 26% (see Table S1†). Thus, the iron added above 0.5% level in the catalyst precursor is present mainly in the form of inorganic iron species rather than FeN_xC_y sites in the final CDC-2-derived catalysts. Comparing the two CDCs, the higher activity of Fe_1–N/CDC-2 than Fe_1–N/CDC-1 likely arises in part from the larger absolute amount of microporous surface area in CDC-2 *vs.* CDC-1 and the nearly twice higher amount of micropore volume (see Fig. S1† and 2). For comparison with similar Fe content in the catalysts, the samples $Fe_{0.5}$–N/CDC-2 and Fe_1–N/CDC-1 should be compared (see Table 3). This comparison also reveals a much higher activity for the CDC-2 derived material. Other factors, such as the structural differences and Fe speciation differences coming from the increased content of iron or larger nitrogen content of the catalyst containing less Fe, could also be contributing factors to the increase in kinetic current density.

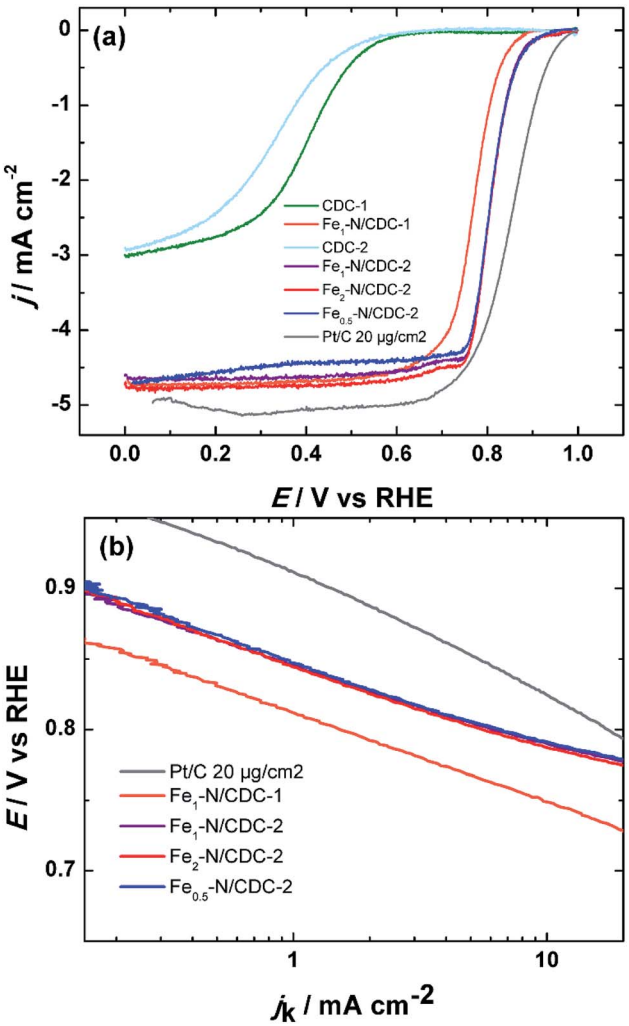

Fig. 7 (a) ORR polarisation curves (not corrected for iR) measured with RDE method for undoped CDCs, B_4C-derived and TiC-derived catalysts in O_2-saturated 0.5 M H_2SO_4. $\nu = 10$ mV s^{-1}, $\omega = 1600$ rpm. (b) Tafel plots calculated from the RDE data shown in (a). Catalyst loading = 803 μg cm^{-2}, except Pt/C (20 μg_{Pt} cm^{-2}).

Table 3 Content of Fe, B, Ti and Zr in the Fe–N/CDC catalysts determined by ICP-MS

Sample	Fe wt%	B wt%	Ti wt%	Zr wt%
Fe_1–N/CDC-1	0.638	1.462	0.079	7.782
Fe_1–N/CDC-2	1.242	n.a	0.148	0.192
Fe_2–N/CDC-2	1.449	n.a	0.120	0.059
$Fe_{0.5}$-N/CDC-2	0.490	0.120	0.06	1.640

Table 4 Kinetic parameters for O_2 reduction on CDC-based catalysts and other state-of-the-art Fe–N–C catalysts in acidic media

Catalyst	$j_{k,(0.8\ V\ vs.\ RHE)}$ (mA cm^{-2})	Catalyst loading (mg cm^{-2})	MA at 0.8 V (A g_{Fe-N-C}^{-1})	$E_{1/2}$ (V *vs.* RHE)	Reference
CDC-1	0.0	0.8	0	0.40	This work
Fe_1–N/CDC-1	1.5	0.8	1.9	0.77	This work
CDC-2	0.0	0.8	0	0.33	This work
Fe_1–N/CDC-2	5.9	0.8	7.4	0.81	This work
Fe_2–N/CDC-2	5.2	0.8	6.5	0.81	This work
$Fe_{0.5}$-N/CDC-2	6.4	0.8	8.0	0.81	This work
Pt/C (20 μg cm^{-2})	17.2	0.4	—	0.85	This work
Fe–NCB	4.6	0.6	7.7	0.8	27
FePhen@MOF–$ArNH_3$	2.9[a]	0.6	4.7[a]	0.77	13
$Fe_{0.5}$	1.0[a]	0.818	1.2[a]	0.73[a]	11
Fe–N–C–Phen–PANI	3.8[a]	0.6	6.3[a]	0.8	31
FeSAs/PTF-400	1.7[a]	0.2	8.5[a]	0.75[a]	62
(Fe,Co)/N–C	4.1	1.095	3.74	0.86	63
Fe_{SA}–N–C	3.2[a]	0.28	11.5[a]	0.78	64
Fe-ZIF	21.4[a]	0.8	26.8[a]	0.85	65
Fe_2–Z8–C	6.6[a]	0.4	16.5[a]	0.8	66
SA–Fe/NG	5.0[a]	0.6	8.3[a]	0.8	67

[a] Indicates values estimated from figures.

The apparent correlation between activity and micropore SSA may also be a consequence of the different Fe speciation during pyrolysis, metallic Fe particles (present in highly loaded samples) leading to partial graphitization and thus to decreased microporous SSA. For ORR in acid medium, Fe particles encapsulated in carbon are generally accepted to be less active (on a metal-atom basis) than surface Fe–N_x sites.

Also of note is the introduction of ZrO_2 into Fe_1–N/CDC-1, which was not present in high concentration in the catalysts derived from CDC-2. The introduction of ZrO_2 seems to result from the combination of milling process and residual presence of hard B_4C in CDC-1. The presence of B_4C in CDC-1 probably also explains the different Fe speciation seen in the CDC-1 derived Fe–N–C catalyst, with a major content of FeB (Fig. 5a).

Fig. 8 shows the results of stability testing on $Fe_{0.5}$–N/CDC-2. As seen, 10 000 cycles between 0.925 and 0.6 V *vs.* RHE have no effect on the onset potential, while the shape of the polarisation curve and $E_{1/2}$ are minimally influenced. The kinetic current density at 0.8 V was reduced by 29% during 10 000 CVs in 0.5 M H_2SO_4, showing that there is some loss of activity in the kinetic region. The small loss in activity is possibly due to the dissolution of small amounts of Fe species with a lower durability in acid media which were noted from the Mössbauer spectra, or to a slight change in Tafel slope.

The electrocatalytic activity of the three CDC-2 based catalysts toward the ORR in acid media is comparable to some of the best Fe–N–C catalysts found in the literature.[11,12,31,34,56] Within the series of 3 catalysts derived from CDC-2, there is some correlation between (i) activity and specific surface area, and (ii) between activity and micropore volume, as shown in Fig. S2.† As the Mössbauer spectra also showed for CDC-2 derived catalysts, increasing the iron content did not introduce a much larger amount of Fe–N_x sites, but rather increased the amount of γ-iron, iron carbides and α-iron. Since the increase of these crystallographic iron species did not positively affect the electrocatalytic activity of the catalysts toward oxygen reduction, it can be derived that the ORR activity of the Fe–N/CDC materials originates mainly from FeN_xC_y moieties (doublet component D1 or D2, or some of these two doublet components). Because iron particles, especially those not perfectly covered by carbon layers, can create problems in PEMFC by releasing iron ions and promoting the Fenton's reaction,[57] it is therefore preferable to select the catalyst with lower iron loading, *i.e.* $Fe_{0.5}$–N/CDC-2, and showing the highest electrocatalytic activity (Fig. S2†).

The same trend of higher activity for CDC-2 derived materials *vs.* CDC-1 derived materials was observed in fuel cell measurements, as shown in Fig. 9. The catalysts derived from CDC-2 resulted in *ca.* 3–4 times higher current density at 0.8 V cell voltage (5–6 *vs.* 20 mA cm^{-2}), whereas the current density in RDE was nearly 5 times higher at 0.8 V. Most of the active sites in these materials are also likely located deep inside the catalyst grains as the Fe content determined by ICP-MS is much higher than on the surface, since iron was not even detected by XPS. It is obviously not optimal to have most of the active sites located deep inside a microporous particle, where the access by O_2 is difficult.[58,59] The power performance at 0.6 V could possibly be improved by decreasing the grain size of the catalyst, either by starting off with a finer carbide or ball-milling the CDC using a high rotation rate, liquid ball-milling or even surfactants in the milling mixture, all of which are known to be useful for obtaining smaller particle sizes[60] or optimising the PEMFC cathode catalyst layer. The results for 5 wt% Pt/C are also shown in the Fig. 9, which are performance-wise not very far from the Fe–N-CDCs. The Pt loading on the cathode was 80 μg_{Pt} cm^{-2}. Assuming the most active sites for ORR in acid medium are represented by the two doublets in Mössbauer spectroscopy (assigned to FeN_x sites), and assessing the bulk density of FeN_x sites by multiplying the fraction of (D1 + D2)

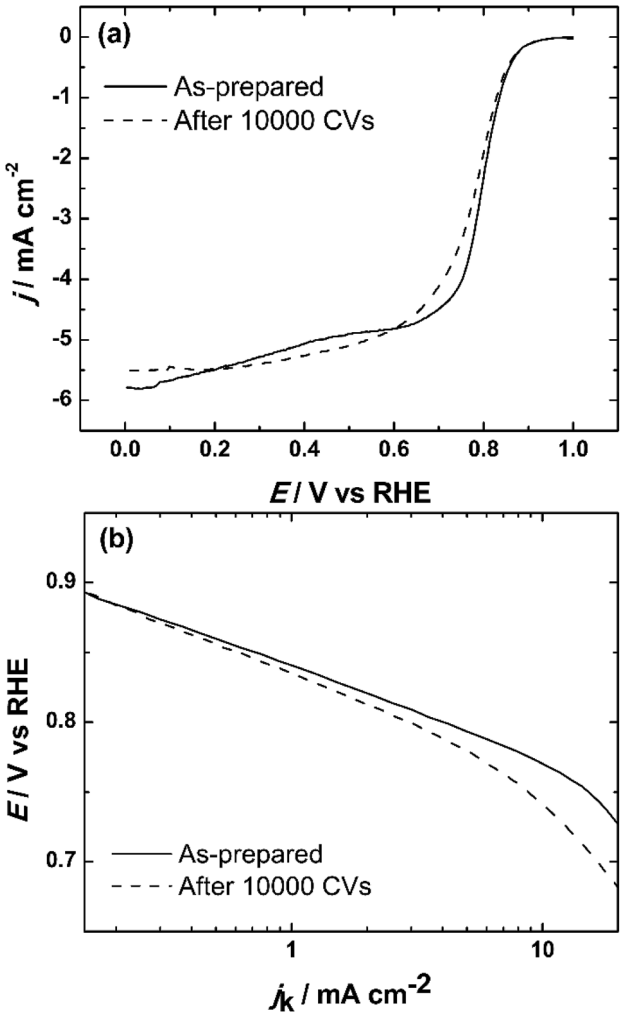

Fig. 8 (a) ORR polarisation curves of $Fe_{0.5}$–N/CDC-2-modified GC electrodes in O_2-saturated 0.5 M H_2SO_4 before and after 10 000 CVs. ν = 10 mV s^{-1}, ω = 1600 rpm. (b) Tafel plots calculated from the RDE data shown in (a).

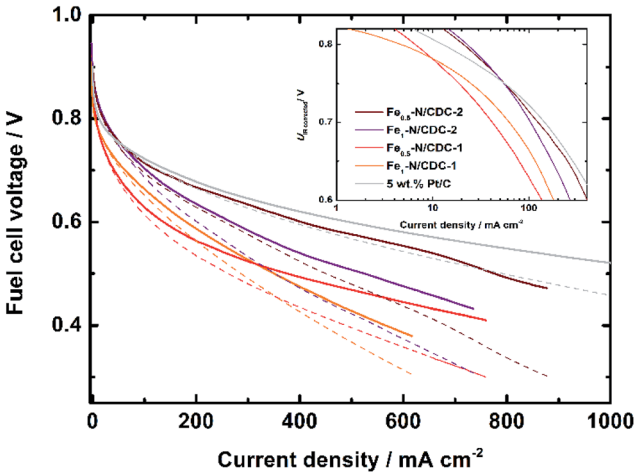

Fig. 9 PEMFC polarisation curves with cathodes comprising 4 mg cm^{-2} of Fe–N–C catalysts, as-measured (dashed curves) and after iR-correction (solid curves). The fuel cell temperature was 80 °C, pure O_2 and H_2 gases were humidified at 100% RH at cell temperature, the gas pressure was 1 bar. Inset: Tafel plots at high potential of iR-free polarisation curves.

from Mössbauer table by the bulk Fe contents measured by ICP-MS, one gets the following numbers: 0.24 wt% ($Fe_{0.5}$–N/CDC-2), 0.54 wt% (Fe_1–N/CDC-2) and 0.38 wt% (Fe_2–N/CDC-2) of Fe–N_x. Considering the significant differences in elemental composition, iron species, porosity and structure, the ORR activity for the Fe_x–N/CDC-2 catalysts is remarkably similar. Elucidating this further would, however, require a thorough study on the kinetics of the ORR on these catalysts and quantification of available active sites, which is outside the scope of the present work.

Compared to the best results for PEMFCs in the literature the current densities achieved by the Fe–N/CDC catalysts presented here might not seem much, but one has to make certain considerations. Serov *et al.* used the sacrificial silica templating method with nicarbazin acting as the nitrogen and carbon source[27] and achieved $E_{1/2}$ of 0.8 V *vs.* RHE in 0.5 M H_2SO_4, which is comparable to the best Fe–N/CDC catalysts studied in this work. However, their Fe–nicarbazin-derived catalyst performed better in PEMFC. The current density in a PEMFC single cell at 0.8 V was 100 mA cm^{-2} using the catalyst studied by Serov *et al.* when compared to 20 mA cm^{-2} achieved in this work. The morphology of the catalyst presented in that work, however, was quite different from the CDC-based ones presented here as it seems to form a network rather than particles. Another highly active catalyst with no FeN_xC_y sites synthesized by Strickland *et al.*[13] showed a half-wave potential that was actually lower than that of the best Fe–N/CDC catalyst here, but in fuel cell testing the current densities reached were again much higher: at 0.6 V the current densities reached in that study were around 750 mA cm^{-2}, while the best catalyst presented here achieved only 400 mA cm^{-2} at a potential of 0.6 V. The specific surface area for the best FePhen@MOF catalyst presented in that work was around 1200 m^2 g^{-1}, similar to 1009 m^2 g^{-1} of $Fe_{0.5}$–N/CDC-2, but the particle size was much smaller, with most particles on the SEM images presented there under 100 nm in diameter at least, compared to the micrometre-sized CDC particles. Also, the presence of CNTs between the particles may have helped in creating macropores in the cathode layer, which might help removing water or improving gas diffusion at high current densities. The most active Fe–N–C material reported by Zitolo *et al.* that contained only FeN_xC_y sites, synthesized with a method similar to the one used here but with a MOF instead of CDCs and subjected to a second pyrolysis in NH_3,[11] was however more active in both RDE and PEMFC testing. Prior to NH_3 activation, however, the same catalyst had a current density of around 175 mA cm^{-2} at 0.6 V, which is much less than that of $Fe_{0.5}$–N/CDC-2. A highly active catalyst recently reported by Fu *et al.*, which was essentially a composite of a 1,10-phenanthroline and Fe-doped Ketjenblack carbon and polyaniline-derived nitrogen and iron-containing carbon, also showed similar activities in an RDE test, with the half-wave potential of 0.8 V *vs.* RHE, but shadowed the CDC-based catalysts in PEMFCs[31] with a kinetic current density of 390 mA cm^{-2} at 0.8 V. The porosity

characteristics were again similar to the most active CDC-based materials, but the particle size was smaller, with some particles visible between a graphene-like structure. It is noteworthy that all CDC-derived catalysts showed lower power performance at 0.6 V compared to some of the highest reported values with Fe–N–C cathodes we discussed here: the power density at 0.6 V with $Fe_{0.5}$–N/CDC-2 as the cathode catalyst was 243 mW cm^{-2} compared to around 800 mW cm^{-2} in the literature.[31] However, one has to take into account that all of the best catalysts in the literature have been heat-treated in ammonia (either on a first stage or in a second, shorter, pyrolysis). This increases the activity notably but is generally known to be detrimental to the stability of such catalysts.[11,61] In the study by Zitolo *et al.*, an NH_3-activated Fe–N–C catalyst showed very fast deactivation over the first 10 h of operation and lost overall more than half of its current density during a 50 hour potentiostatic test at 0.5 V, while the Ar-pyrolysed Fe–N–C catalyst was relatively stable. After 50 h operation at 0.5 V, the current density at 0.5 V of the NH_3-activated Fe–N–C catalyst in that study was actually similar to that initially achieved by $Fe_{0.5}$–N/CDC-2 in the present study (500 and 450 mA cm^{-2}, respectively). The activity and power performance of the Fe–N–C catalysts derived from CDC-2 and pyrolysed in argon are, compared to other state-of-art Fe–N–C catalysts pyrolysed in inert gas, equivalent or even superior.

4. Conclusions

Two carbide-derived carbons with well-defined but different pore size distributions were investigated as pure microporous or micro–mesoporous host matrices to synthesize FeN_xC_y moieties for O_2 electroreduction. It is concluded that the carbide-derived carbon comprising only micropores resulted in more active Fe–N–C catalysts for oxygen electroreduction in acid medium. This difference in the ORR activity of Fe–N–C catalysts prepared from different CDCs is explained by the preferential formation of ORR-active FeN_xC_y moieties in the pure microporous CDC, as observed by Mössbauer spectroscopy. For the micro-mesoporous CDC, the residual presence of boron seems to have triggered the formation of ORR-inactive iron boride, with consequently lower amount of FeN_xC_y moieties. These first results on the use of CDC for preparing Fe–N–C catalysts for PEMFC application are highly promising. The exact micropore size in starting CDCs can be further optimised in the future (can be tuned with the starting carbide used and synthesis conditions), and the grain size can also be optimised. The complete removal of chemical elements from the starting carbide template seems also an important aspect, at least for boron carbide. For optimising performance in PEMFC, these ORR-active domains with only micropores could also be combined with more advanced preparation methods for cathode layer, with hierarchical micro and macropores for maximizing the number of active sites and their accessibility by O_2, respectively.

Conflicts of interest

There are no conflicts to declare.

Acknowledgements

The present work was financially supported by institutional research funding (IUT20-16 and IUT34-14) of the Estonian Ministry of Education and Research. This research was also supported by the EU through the European Regional Development Fund (TK141, "Advanced materials and high-technology devices for energy recuperation systems"). SR would like to thank the Erasmus+ programme for the scholarship to study at Université de Montpellier. Use of Beamline ISS 8-ID of the National Synchrotron Light Source (NSLS) II was supported by the NSLS-II, Brookhaven National Laboratory, under U.S. DOE Contract No. DE-SC0012704.

Notes and references

1 O. Gröger, H. A. Gasteiger and J.-P. Suchsland, *J. Electrochem. Soc.*, 2015, **162**, A2605–A2622.
2 C. E. Thomas, *Int. J. Hydrogen Energy*, 2009, **34**, 6005–6020.
3 M. K. Debe, *Nature*, 2012, **486**, 43–51.
4 I. Katsounaros, S. Cherevko, A. R. Zeradjanin and K. J. J. Mayrhofer, *Angew. Chem., Int. Ed.*, 2014, **53**, 102–121.
5 F. Jaouen, E. Proietti, M. Lefèvre, R. Chenitz, J.-P. Dodelet, G. Wu, H. T. Chung, C. M. Johnston and P. Zelenay, *Energy Environ. Sci.*, 2011, **4**, 114–130.
6 J.-P. Dodelet, Z. Chen and J. Zhang, *Non-nobel metal fuel cell catalysts*, Wiley, Weinheim, Germany, 2014.
7 M. Shao, Q. Chang, J.-P. Dodelet and R. Chenitz, *Chem. Rev.*, 2016, **116**, 3594–3657.
8 J. H. Zagal and F. Bedioui, *Electrochemistry of N4 macrocyclic metal complexes: Volume 1: Energy, second edition*, Springer International Publishing, Cham, 2nd edn., 2016.
9 M. Lefèvre, E. Proietti, F. Jaouen and J. P. Dodelet, *Science*, 2009, **324**, 71–74.
10 F. Jaouen, J. Herranz, M. Lefévre, J. P. Dodelet, U. I. Kramm, I. Herrmann, P. Bogdanoff, J. Maruyama, T. Nagaoka, A. Garsuch, J. R. Dahn, T. Olson, S. Pylypenko, P. Atanassov and E. A. Ustinov, *ACS Appl. Mater. Interfaces*, 2009, **1**, 1623–1639.
11 A. Zitolo, V. Goellner, V. Armel, M. T. Sougrati, T. Mineva, L. Stievano, E. Fonda and F. Jaouen, *Nat. Mater.*, 2015, **14**, 937–942.
12 Q. Jia, N. Ramaswamy, U. Tylus, K. Strickland, J. Li, A. Serov, K. Artyushkova, P. Atanassov, J. Anibal, C. Gumeci, S. C. Barton, M. T. Sougrati, F. Jaouen, B. Halevi and S. Mukerjee, *Nano Energy*, 2016, **29**, 65–82.
13 K. Strickland, E. Miner, Q. Jia, U. Tylus, N. Ramaswamy, W. Liang, M. T. Sougrati, F. Jaouen and S. Mukerjee, *Nat. Commun.*, 2015, **6**, 7343.
14 L. Dai, Y. Xue, L. Qu, H.-J. Choi and J.-B. Baek, *Chem. Rev.*, 2015, **115**, 4823–4892.
15 N. Daems, X. Sheng, I. F. J. Vankelecom and P. P. Pescarmona, *J. Mater. Chem. A*, 2014, **2**, 4085–4110.
16 G. A. Ferrero, K. Preuss, A. B. Fuertes, M. Sevilla and M.-M. Titirici, *J. Mater. Chem. A*, 2016, **4**, 2581–2589.
17 N. Ramaswamy, U. Tylus, Q. Jia and S. Mukerjee, *J. Am. Chem. Soc.*, 2013, **135**, 15443–15449.

18 K. Artyushkova, A. Serov, S. Rojas-Carbonell and P. Atanassov, *J. Phys. Chem. C*, 2015, **119**, 25917–25928.
19 A. Sarapuu, E. Kibena-Põldsepp, M. Borghei and K. Tammeveski, *J. Mater. Chem. A*, 2018, **6**, 776–804.
20 A. A. Gewirth, J. A. Varnell and A. M. DiAscro, *Chem. Rev.*, 2018, **118**, 2313–2339.
21 C. H. Choi, W. S. Choi, O. Kasian, A. K. Mechler, M. T. Sougrati, S. Brüller, K. Strickland, Q. Jia, S. Mukerjee, K. J. J. Mayrhofer and F. Jaouen, *Angew. Chem., Int. Ed.*, 2017, **56**, 8809–8812.
22 F. Charreteur, S. Ruggeri, F. Jaouen and J. P. Dodelet, *Electrochim. Acta*, 2008, **53**, 6881–6889.
23 F. Jaouen, M. Lefèvre, J. P. Dodelet and M. Cai, *J. Phys. Chem. B*, 2006, **110**, 5553–5558.
24 U. I. Kramm, M. Lefèvre, N. Larouche, D. Schmeisser and J. P. Dodelet, *J. Am. Chem. Soc.*, 2014, **136**, 978–985.
25 V. Armel, S. Hindocha, F. Salles, S. Bennett, D. Jones and F. Jaouen, *J. Am. Chem. Soc.*, 2017, **139**, 453–464.
26 B. Y. Xia, Y. Yan, N. Li, H. Bin Wu, X. W. Lou and X. Wang, *Nat. Energy*, 2016, **1**, 15006.
27 A. Serov, K. Artyushkova, E. Niangar, C. Wang, N. Dale, F. Jaouen, M. T. Sougrati, Q. Jia, S. Mukerjee and P. Atanassov, *Nano Energy*, 2015, **16**, 293–300.
28 G. Wu, K. L. More, C. M. Johnston and P. Zelenay, *Science*, 2011, **332**, 443–447.
29 V. Nallathambi, J. W. Lee, S. P. Kumaraguru, G. Wu and B. N. Popov, *J. Power Sources*, 2008, **183**, 34–42.
30 S. Gupta, S. Zhao, O. Ogoke, Y. Lin, H. Xu and G. Wu, *ChemSusChem*, 2017, **10**, 774–785.
31 X. Fu, P. Zamani, J. Y. Choi, F. M. Hassan, G. Jiang, D. C. Higgins, Y. Zhang, M. A. Hoque and Z. Chen, *Adv. Mater.*, 2017, **29**, 1604456.
32 J. A. Varnell, J. S. Sotiropoulos, T. M. Brown, K. Subedi, R. T. Haasch, C. E. Schulz and A. A. Gewirth, *ACS Energy Lett.*, 2018, **3**, 823–828.
33 J. Shui, C. Chen, L. Grabstanowicz, D. Zhao and D.-J. Liu, *Proc. Natl. Acad. Sci. U. S. A.*, 2015, **112**, 10629–10634.
34 J. Li, S. Ghoshal, W. Liang, M.-T. Sougrati, F. Jaouen, B. Halevi, S. McKinney, G. McCool, C. Ma, X. Yuan, Z.-F. Ma, S. Mukerjee and Q. Jia, *Energy Environ. Sci.*, 2016, **9**, 2418–2432.
35 M. Ferrandon, A. J. Kropf, D. J. Myers, K. Artyushkova, U. Kramm, P. Bogdanoff, G. Wu, C. M. Johnston and P. Zelenay, *J. Phys. Chem. C*, 2012, **116**, 16001–16013.
36 Y. Zhai, Y. Dou, D. Zhao, P. F. Fulvio, R. T. Mayes and S. Dai, *Adv. Mater.*, 2011, **23**, 4828–4850.
37 R. K. Dash, G. Yushin and Y. Gogotsi, *Microporous Mesoporous Mater.*, 2005, **86**, 50–57.
38 A. Jänes, T. Thomberg, H. Kurig and E. Lust, *Carbon*, 2009, **47**, 23–29.
39 A. Jänes, L. Permann, M. Arulepp and E. Lust, *Electrochem. Commun.*, 2004, **6**, 313–318.
40 M. Schmirler, T. Knorr, T. Fey, A. Lynen, P. Greil and B. J. M. Etzold, *Carbon*, 2011, **49**, 4359–4367.
41 S. Ratso, I. Kruusenberg, M. Käärik, M. Kook, R. Saar, M. Pärs, J. Leis and K. Tammeveski, *Carbon*, 2017, **113**, 159–169.
42 M. Käärik, M. Arulepp, M. Kook, U. Mäeorg, J. Kozlova, V. Sammelselg, A. Perkson and J. Leis, *J. Porous Mater.*, 2018, **25**, 1057–1070.
43 S. Kabir, K. Artyushkova, A. Serov, B. Kiefer and P. Atanassov, *Surf. Interface Anal.*, 2016, **48**, 293–300.
44 K. Artyushkova, I. Matanovic, B. Halevi and P. Atanassov, *J. Phys. Chem. C*, 2017, **121**, 2836–2843.
45 A. L. Ankudinov, B. Ravel, J. J. Rehr and S. D. Conradson, *Phys. Rev. B: Condens. Matter Mater. Phys.*, 1998, **58**, 7565–7576.
46 T. Sun, L. Xu, S. Li, W. Chai, Y. Huang, Y. Yan and J. Chen, *Appl. Catal., B*, 2016, **193**, 1–8.
47 J. Y. Cheon, T. Kim, Y. Choi, H. Y. Jeong, M. G. Kim, Y. J. Sa, J. Kim, Z. Lee, T. H. Yang, K. Kwon, O. Terasaki, G. G. Park, R. R. Adzic and S. H. Joo, *Sci. Rep.*, 2013, **3**, 2715.
48 H. W. Liang, W. Wei, Z. S. Wu, X. Feng and K. Müllen, *J. Am. Chem. Soc.*, 2013, **135**, 16002–16005.
49 M. Käärik, M. Arulepp, M. Karelson and J. Leis, *Carbon*, 2008, **46**, 1579–1587.
50 J. Leis, A. Perkson, M. Arulepp, P. Nigu and G. Svensson, *Carbon*, 2002, **40**, 1559–1564.
51 S. Ratso, I. Kruusenberg, M. Käärik, M. Kook, R. Saar, P. Kanninen, T. Kallio, J. Leis and K. Tammeveski, *Appl. Catal., B*, 2017, **219**, 276–286.
52 A. Garsuch, R. Yang, A. Bonakdarpour and J. R. Dahn, *Electrochim. Acta*, 2008, **53**, 2423–2429.
53 J. D. Cooper, T. C. Gibb, N. N. Greenwood and R. V. Parish, *Trans. Faraday Soc.*, 1964, **60**, 2097–2104.
54 T. Kanaizuka, *Phys. Status Solidi A*, 1982, **69**, 739–744.
55 N. Markovic, H. A. Gasteiger and P. N. Ross, *J. Electrochem. Soc.*, 1997, **144**, 1591–1597.
56 Y. Chen, R. Gokhale, A. Serov, K. Artyushkova and P. Atanassov, *Nano Energy*, 2017, **38**, 201–209.
57 D. Banham, S. Ye, K. Pei, J. I. Ozaki, T. Kishimoto and Y. Imashiro, *J. Power Sources*, 2015, **285**, 334–348.
58 L. Yang, N. Larouche, R. Chenitz, G. Zhang, M. Lefèvre and J. P. Dodelet, *Electrochim. Acta*, 2015, **159**, 184–197.
59 G. Zhang, R. Chenitz, M. Lefèvre, S. Sun and J. P. Dodelet, *Nano Energy*, 2016, **29**, 111–125.
60 C. Suryanarayana, *Prog. Mater. Sci.*, 2001, **46**, 1–184.
61 R. Chenitz, U. I. Kramm, M. Lefevre, V. Glibin, G. Zhang, S. Sun and J.-P. Dodelet, *Energy Environ. Sci.*, 2018, **11**, 365–382.
62 J.-D. Yi, R. Xu, Q. Wu, T. Zhang, K.-T. Zang, J. Luo, Y.-L. Liang, Y.-B. Huang and R. Cao, *ACS Energy Lett.*, 2018, **3**, 883–889.
63 J. Wang, Z. Huang, W. Liu, C. Chang, H. Tang, Z. Li, W. Chen, C. Jia, T. Yao, S. Wei, Y. Wu and Y. Li, *J. Am. Chem. Soc.*, 2017, **139**, 17281–17284.
64 L. Jiao, G. Wan, R. Zhang, H. Zhou, S.-H. Yu and H.-L. Jiang, *Angew. Chem., Int. Ed.*, 2018, **57**, 8525–8529.
65 H. Zhang, S. Hwang, M. Wang, Z. Feng, S. Karakalos, L. Luo, Z. Qiao, X. Xie, C. Wang, D. Su, Y. Shao and G. Wu, *J. Am. Chem. Soc.*, 2017, **139**, 14143–14149.
66 Q. Liu, X. Liu, L. Zheng and J. Shui, *Angew. Chem., Int. Ed.*, 2018, **57**, 1204–1208.
67 L. Yang, D. Cheng, H. Xu, X. Zeng, X. Wan, J. Shui, Z. Xiang and D. Cao, *Proc. Natl. Acad. Sci. U. S. A.*, 2018, 201800771.

